

Energetic Electrons Accelerated and Trapped in a Magnetic Bottle above a Solar Flare Arcade

BIN CHEN,¹ XIANGLIANG KONG,² SIJIE YU,¹ CHENGCAI SHEN,³ XIAOCAN LI,⁴ FAN GUO,⁵ YIXIAN ZHANG,⁶
LINDSAY GLESENER,⁶ AND SÄM KRUCKER^{7,8}

¹Center for Solar-Terrestrial Research, New Jersey Institute of Technology, 323 Martin Luther King Blvd, Newark, NJ 07102-1982, USA

²Institute of Space Sciences, Shandong University, Weihai, Shandong 264209, China

³Harvard-Smithsonian Center for Astrophysics, Cambridge, MA 02138, USA

⁴Department of Physics and Astronomy, Dartmouth College, Hanover, NH 03755, USA

⁵Los Alamos National Laboratory, Los Alamos, NM 87545, USA

⁶School of Physics & Astronomy, University of Minnesota Twin Cities, Minneapolis, MN 55455, USA

⁷Space Sciences Laboratory, University of California, 7 Gauss Way, 94720 Berkeley, USA

⁸University of Applied Sciences and Arts Northwestern Switzerland, 5210 Windisch, Switzerland

ABSTRACT

Where and how flares efficiently accelerate charged particles remains an unresolved question. Recent studies revealed that a “magnetic bottle” structure, which forms near the bottom of a large-scale reconnection current sheet above the flare arcade, is an excellent candidate for confining and accelerating charged particles. However, further understanding its role requires linking the various observational signatures to the underlying coupled plasma and particle processes. Here we present the first study combining multi-wavelength observations with data-informed macroscopic magnetohydrodynamics and particle modeling in a realistic eruptive flare geometry. The presence of an above-the-looptop magnetic bottle structure is strongly supported by the observations, which feature not only a local minimum of magnetic field strength but also abruptly slowing down plasma downflows. It also coincides with a compact hard X-ray source and an extended microwave source that bestrides above the flare arcade. Spatially resolved spectral analysis suggests that nonthermal electrons are highly concentrated in this region. Our model returns synthetic emission signatures that are well-matched to the observations. The results suggest that the energetic electrons are strongly trapped in the magnetic bottle region due to turbulence, with only a small fraction managing to escape. The electrons are primarily accelerated by plasma compression and facilitated by a fast-mode termination shock via the Fermi mechanism. Our results provide concrete support for the magnetic bottle as the primary electron acceleration site in eruptive solar flares. They also offer new insights into understanding the previously reported small population of flare-accelerated electrons entering interplanetary space.

Keywords: Solar flares (1496), Solar energetic particles (1491), Magnetohydrodynamical simulations (1966), Non-thermal radiation sources (1119), Solar radio emission (1522), Solar x-ray emission (1536), Solar extreme ultraviolet emission (1493)

1. INTRODUCTION

The discovery of hard X-ray (HXR) sources located above the bright solar flare arcade (after Masuda et al. Masuda et al. 1994) has convincingly placed the primary flare energy release and particle acceleration site to the coronal volume. It coincides with the location where a large-scale current sheet is present to drive the flare energy release via magnetic reconnection—a process in which magnetic field lines break and reconnect to unleash the previously stored magnetic energy. Owing to its strong electric field that can reach thousands of volts per meter, this reconnection current sheet has

often been suggested as the main driver for particle acceleration (Martens 1988; Litvinenko 1996; Kliem et al. 2000; Drake et al. 2006; Bárta et al. 2011; Li et al. 2018).

However, since energetic particles are extremely mobile in the solar corona, the acceleration of a large number of particles to nonthermal energies requires efficient bulk acceleration, strong trapping, or both. Where and how such bulk acceleration and trapping occur remains an unresolved problem. Moreover, studies that combine *in situ* spacecraft measurements and remote-sensing observations have concluded consistently that only 0.1–1% of the flare-accelerated energetic electrons

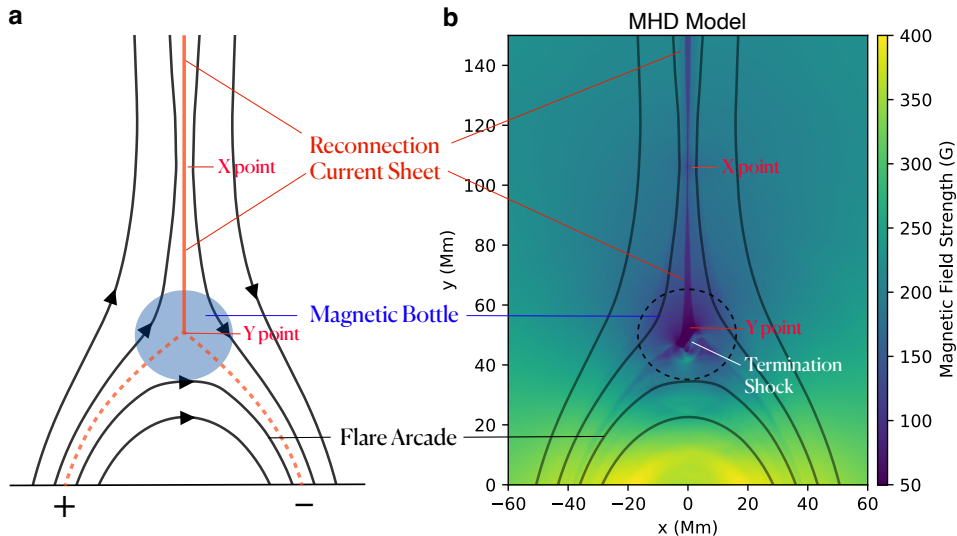


Figure 1. Formation of a magnetic bottle structure above a solar flare arcade. (a) The presence of a large-scale reconnection current sheet above the flare arcade leads to a local divergence of the magnetic field lines in the above-the-looptop region, forming a magnetic bottle (shaded blue ellipse). The vertical red line is the reconnection current sheet, and the dashed red curve denotes the quasi-separatrix layer. (b) The total magnetic field strength distribution in a 2.5-D resistive MHD model shows a generally lower magnetic field strength in the magnetic bottle region. Also marked are the X point where the field lines break and reconnect, the Y point where the current sheet meets the quasi-separatrix layer, and a fast-mode termination shock formed by reconnection outflows impinging upon the flare arcade.

manage to escape to interplanetary space (Lin 1974; Krucker et al. 2007; Dresing et al. 2021; Wang et al. 2021, 2023a). Such a profound departure from equipartition between the upward-escaped and downward-precipitated/trapped energetic electrons at the flare site has posed a significant challenge in understanding the particle acceleration and transport processes.

Previous results based on HXR analysis of the electron time-of-flight distances (Aschwanden et al. 1996a,b) and observations of above-the-looptop (“ALT” hereafter) sources with a high nonthermal electron density (e.g., Krucker et al. 2010; Ishikawa et al. 2011; Krucker & Battaglia 2014; Fleishman et al. 2022) have suggested that the primary acceleration in large eruptive flares may be located in the cusp region just above the flare arcade, but not necessarily in the upper portion of the current sheet, including the primary X point(s). Recently, by combining microwave imaging spectroscopy observations with magnetohydrodynamics (MHD) modeling, Chen et al. (2020b) found that the region near the bottom of the current sheet (also known as the “Y point” owing to the bifurcation of the current layer; see Figure 1(a)) coincides with a local depression of magnetic field strength. This peculiar structure, referred to as a “magnetic bottle,” is a natural consequence of energy release driven by magnetic reconnection in a large-scale, vertical current sheet above the flare arcade. In the schematic picture shown in Figure 1(a), the anti-

parallel magnetic field lines encompassing the current sheet diverge toward the top of the flare arcade. A similar field line divergence is also evident as one follows the footpoints of the flare arcade upward toward the looptop. In turn, the conservation of magnetic flux demands a general reduction of the magnetic field strength in the ALT region. Such a physical picture is supported by analytical models of flare reconnections (Fletcher & Martens 1998; Lin & Forbes 2000) and numerical simulations that solve the magnetohydrodynamics (MHD) equations. Figure 1(b) shows an example frame from our MHD simulations (after Shen et al. 2018), which displays a reduced magnetic field strength at the same region.

This magnetic bottle structure coincides with the location of the ALT HXR source and shows a strong concentration of microwave-emitting nonthermal electrons (Chen et al. 2020b), implicating a key role it may be playing in the particle acceleration processes. This is also where the fast reconnection outflows—which carry the bulk of the released energy—collide head-on against the flare arcade to create a plethora of energetic phenomena such as collapsing magnetic traps (Somov & Kosugi 1997; Karlický & Kosugi 2004), fast-mode termination shocks (Forbes 1986; Tsuneta & Naito 1998; Aurass et al. 2002; Aurass & Mann 2004; Mann et al. 2009; Guo & Giacalone 2012; Chen et al. 2015, 2019; Takasao et al. 2015; Polito et al. 2018; Shen et al. 2018,

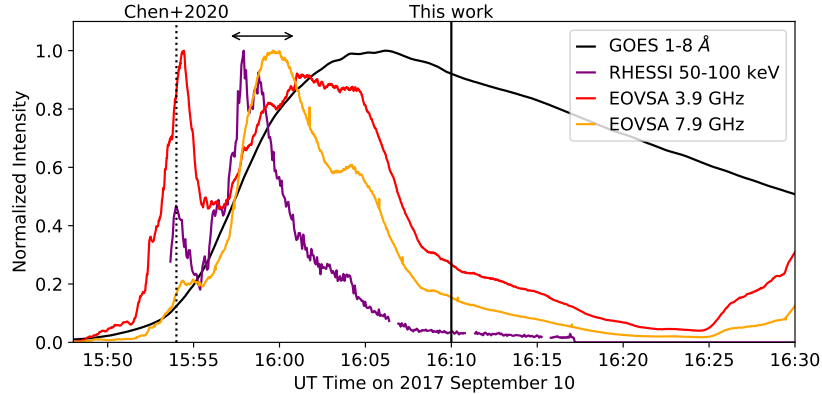


Figure 2. Microwave and X-ray light curves of the X8.2-class eruptive solar flare on 2017 September 10. The solid vertical line indicates the time of interest of this work during the gradual phase of the flare (around 16:10 UT). The vertical dotted line marks the time studied by [Chen et al. \(2020b\)](#) during the early impulsive phase of the flare when the eruption was initiated, and the double-sided arrow denotes the main impulsive phase of the flare around the primary hard X-ray and microwave peak (see [Gary et al. 2018](#) for more details on the flare evolution).

2022; [Ye et al. 2020](#); [Luo et al. 2021](#); [French et al. 2024](#)), slow-mode or gas dynamic shocks ([Reeves et al. 2007](#); [Longcope & Guidoni 2011](#); [Longcope et al. 2016](#); [Longcope & Qiu 2022](#)), as well as turbulence and oscillations ([Takasao & Shibata 2016](#); [Kontar et al. 2017](#); [Reeves et al. 2020](#); [Ye et al. 2020](#); [Shen et al. 2022, 2023](#); [Ruan et al. 2023](#); [Shibata et al. 2023](#); [Wang et al. 2023b](#)), serving as an ideal environment to heat flare plasma and accelerate charged particles.

However, understanding how the local concentration occurs and, in turn, the underlying particle acceleration and transport mechanisms requires a concerted observational–modeling approach that links the various emission features to the highly coupled plasma dynamics and particle processes, which has been heretofore elusive. Here, we use a novel macroscopic MHD and particle model (after [Kong et al. 2019](#)) to produce not only a distribution of thermal plasma in a realistic flare geometry but also a spatially, spectrally, and temporally resolved distribution of energetic electrons throughout the flare region. The model makes it possible, for the first time, to compare the model outputs with multi-wavelength imaging spectroscopy observations that trace both the heated plasma and nonthermal electrons. The paper is organized as follows. Section 2 discusses the multi-wavelength observations and analysis. Section 3 describes the MHD, particle, and emission modeling setup and results. Section 4 put both the observational and modeling results into a coherent physical context and discuss their implications. For the sake of readability, extensive technical details for X-ray and microwave data analysis and numerical modeling are included in the Appendix.

2. OBSERVATIONS

The observations were obtained during the well-observed X8.2-class eruptive solar flare on 2017 September 10, recorded by ground- and space-based instruments at multiple wavelengths. This event, thanks to its favorable viewing perspective, has a geometry that matches very well the standard model of eruptive solar flares ([Figure 3](#)). We refer interested readers to [Chen et al. \(2020a\)](#) and references therein for a more detailed discussion on its three-dimensional (3D) configuration based on multi-wavelength, multi-perspective observations. Briefly, the event is induced by an erupting magnetic flux rope that drives a fast white light coronal mass ejection (CME). Immediately trailing the CME core, a long linear-shaped feature, seen in both white light and EUV, extends down to the top of the bright flare arcade, interpreted as a large-scale reconnection current sheet viewed edge-on ([Warren et al. 2018](#); [Yan et al. 2018](#); [Chen et al. 2020b](#)). The flare arcade anchored at the solar surface displays a cusp shape as observed by the Atmospheric Imaging Assembly onboard the Solar Dynamics Observatory (SDO/AIA; [Lemen et al. 2012](#)) and the EUV Imaging Spectrometer (EIS; [Culhane et al. 2007](#)) onboard Hinode (see [Figures 3\(b\)](#) and [\(c\)](#), respectively). The cusp-shaped flare loops are the signature of highly bent magnetic field lines resulting from ongoing magnetic reconnection in the current sheet, producing fast sunward reconnection outflows (e.g., [Longcope et al. 2018](#); [Hayes et al. 2019](#); [Yu et al. 2020](#)).

In order to carry out the comparison with our combined MHD, particle, and emission model (see [Section 3](#)), we select a period around 16:10 UT during the gradual phase of the eruptive solar flare when the eruption has already propagated to a large distance (i.e., 12 minutes after the main microwave and HXR peak at

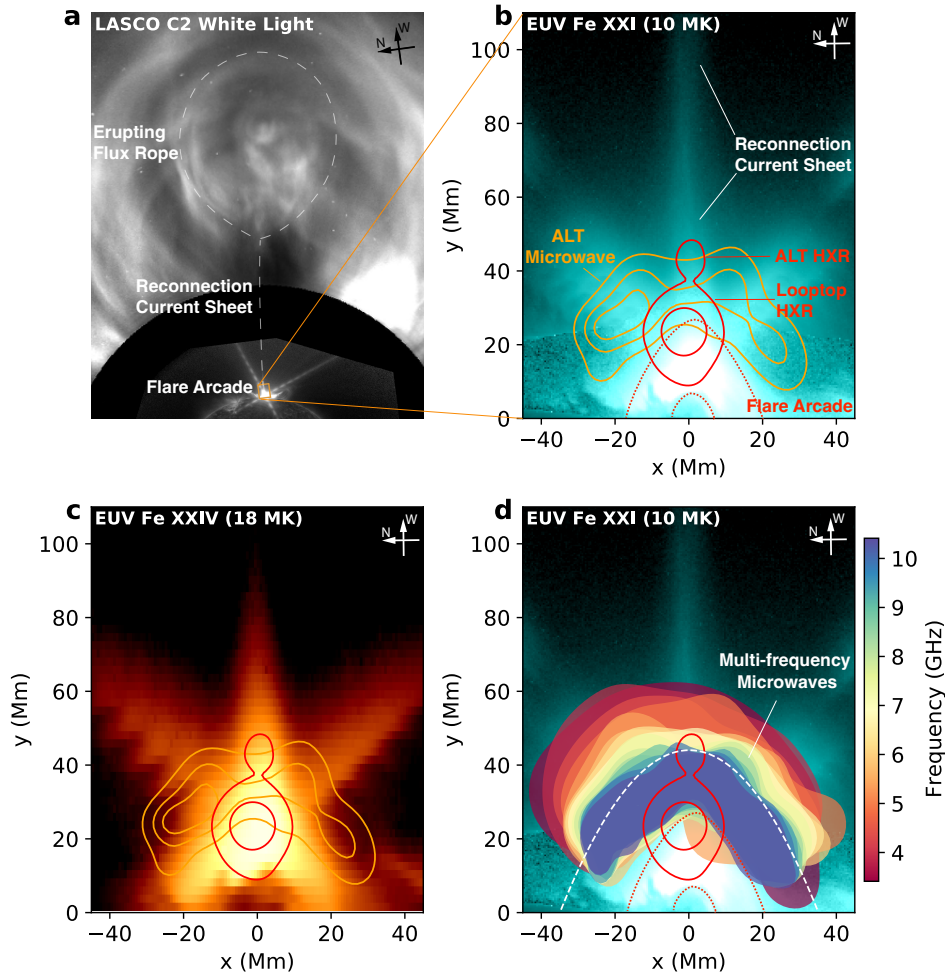


Figure 3. Multi-wavelength observations of the flare during its gradual phase at 16:10 UT. (a) A coronal mass ejection observed in white light by the SOHO/LASCO coronagraph along with a trailing long plasma sheet. Inner inset is the 131 \AA EUV channel image made by the Solar Ultraviolet Imager (SUVI) onboard the GOES-R satellite. (b) Detailed view of the plasma sheet and post-flare arcade region. A small box denotes the field of view in (a). The background is the SDO/AIA 131 \AA EUV channel image, which samples the hot 10 MK plasma through the Fe XXI line, shown with an inverse color scale (i.e., darker color is brighter). Orange contours are the 7.9 GHz microwave source (15%, 50%, and 90% of the maximum). The RHESSI 25–60 keV hard X-ray image is shown as red contours (10% and 50% of the maximum). (c) Same as (b), but the background is the Fe XXIV line EUV image observed by Hinode/EIS, which is sensitive to 18 MK plasma. (d) Similar to (b), but with filled contours denoting multi-frequency EOVSA microwave images from 3.4 GHz to 12.9 GHz.

around 15:58 UT; Figure 2). As shown in Figure 3(a), the core of the white light CME is located at ~ 4 solar radii, followed by a long trailing plasma sheet. In comparison, the size of the flare arcade itself is only ~ 20 Mm, or $\sim 1\%$ of the length of the sheet. Therefore, the plasma processes near the solar surface can be well approximated by a system driven by an infinitely long current sheet as depicted in Figure 1, which allows us to perform detailed data–model comparison in a realistic flare geometry.

We note that the flare event occurred on the west solar limb, and the eruption generally proceeded along the east-west direction. For the sake of easier data-model

comparison, throughout this paper, we have rotated the observed images by 90 degrees counter-clockwise and assigned $x = 950''$ and $y = -140''$ in the original Helioprojective Cartesian coordinates as the origin of our new coordinate system. The length units are in megameters, with $1'' \approx 0.73$ Mm at a distance of 1 AU.

2.1. X-ray and Microwave Imaging and Spectroscopy

In the X-ray images obtained by the Reuven Ramaty High Energy Solar Spectroscopic Imager (RHESSI; Lin et al. 2002), this period features an ALT HXR source at 25–60 keV (Figure 3(b); see also Figure 11 in Appendix for images at additional energy bands). At the top of the

EUV flare arcade, a brighter X-ray source is present (referred to as the “looptop” source), which is dominated by thermal bremsstrahlung from hot (>15 MK) plasma with a high density ($\sim 10^{12}$ cm $^{-3}$). In the total-flux X-ray spectrum, at above ~ 30 keV, a nonthermal component dominates the spectrum with a power-law shape (Figure 4). Spectral analysis suggests that if this component falls into the thin-target bremsstrahlung regime, it corresponds to a total nonthermal electron density of $n_e^{>50} \approx 4 \times 10^6$ cm $^{-3}$ above 50 keV (see detailed discussions in Appendix Section A).

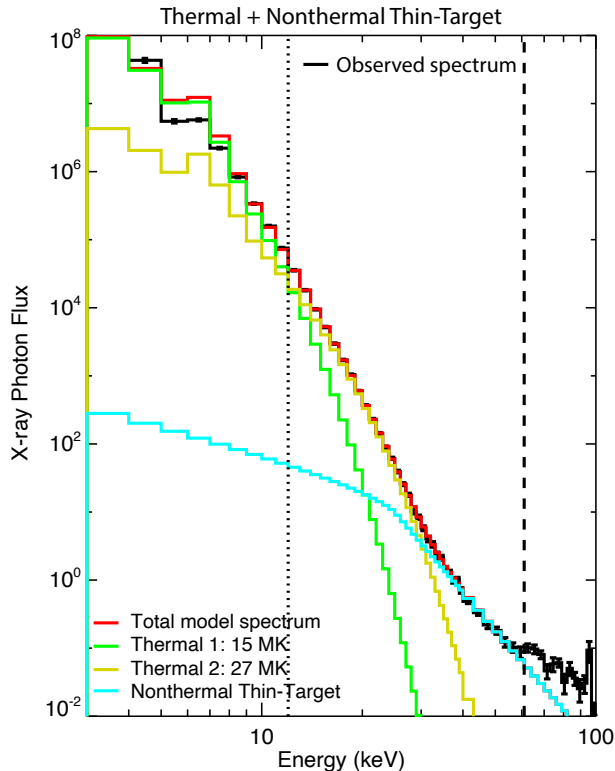


Figure 4. RHESSI X-ray spectral analysis results for the time of interest at 16:10 UT. (a) Black curve represents the observed X-ray photon spectrum averaged over 16:10:00 UT and 16:11:08 UT. The red curve is the best-fit spectrum that includes two isothermal components and one nonthermal component arising from thin-target bremsstrahlung from a power-law electron distribution. The two thermal components, shown as the green and yellow curves, have temperatures of 15 MK and 27 MK, and volume emission measures of 1.6×10^{51} cm $^{-3}$ and 4.1×10^{49} cm $^{-3}$, respectively. The nonthermal thin-target component has a normalization factor of 1.6×10^{54} cm $^{-2}$ s $^{-1}$ with a power-law index of $\delta^{\text{thin}} = 4.7$.

In the microwave images observed by the Expanded Owens Valley Solar Array (EOVSA; Gary et al. 2018) in 2.5–18 GHz, no counterpart of the bright looptop X-ray

source is present. Instead, it features an arcade-shaped source that bestrides above the bright EUV flare arcade (orange contours in Figure 3). The arcade-shaped source can be clearly seen in microwave images at all frequencies, with subtle changes in their appearance (left panels in Figure 5). Interestingly, the low-frequency images ($\lesssim 6$ GHz) display a small “gap” at the central location (i.e., near $x = 0$ Mm) with a relatively lower brightness temperature. With EOVSA’s multi-frequency imaging capability, one can derive microwave spectra from different locations of the images and perform spectral analysis. In Figure 6(a), we show a frequency–space spectrogram obtained along a fiducial slit drawn along the spine of the microwave arcade passing the ALT HXR source at $x \approx 0$ Mm (dashed curve in Figure 3(d)). Such a spectrogram is akin to those obtained by slit spectrographs, with the microwave intensity along the slit “dispersed” in frequency over the vertical axis. Figure 6(b) show microwave brightness temperature spectra derived from five equally spaced locations along the slit. All spectra show a positive spectral slope at low frequencies and a negative slope at high frequencies with a peak brightness temperature of ~ 100 MK, consistent with gyrosynchrotron emission produced by nonthermal electrons gyrating in the coronal magnetic field (e.g., Dulk & Marsh 1982). The spectral properties are primarily sensitive to parameters of the nonthermal electron distribution and the magnetic field in the source.

Following Chen et al. (2020b), we use the Markov chain Monte Carlo (MCMC) method to analyze the observed spectra (see Appendix Section B for details). Figure 6(c) shows the distribution of the best-fit magnetic field strength B along the slit. It displays a local minimum of B at the center of the slit around $x \approx 0$ Mm, suggestive of a magnetic bottle structure co-located with the ALT HXR source. Meanwhile, despite the relatively large uncertainties, the distribution of the total nonthermal electron density above 50 keV $n_e^{>50}$ (Figure 6(d)) indicates that the best-fit value in the central magnetic bottle region is two orders of magnitude greater than locations into the loop legs at $|x| > 20$ Mm, implying that microwave-emitting nonthermal electrons are strongly concentrated in the magnetic bottle region. The best-fit nonthermal electron density in the magnetic bottle region is also consistent with that returned from the X-ray spectral analysis within uncertainties.

2.2. EUV Plasma Downflows

In the ALT magnetic bottle region, the magnetic field lines associated with the downward reconnection outflows are expected to start from a nearly anti-parallel configuration in the reconnection current sheet to a

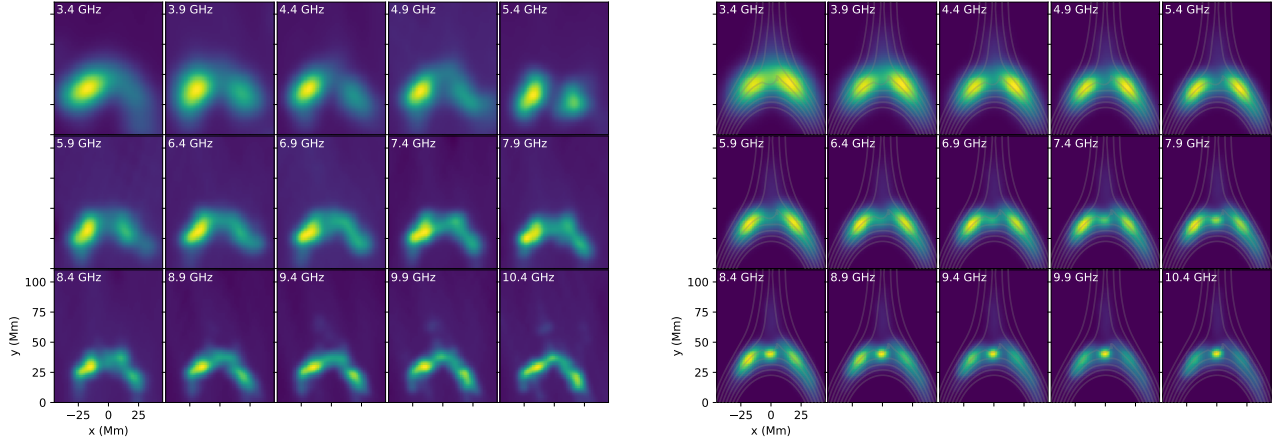


Figure 5. Observed and modeled multi-frequency microwave images from 3.4 GHz to 10.4 GHz. Left panels: Microwave images observed by EOVSA on 2017 September 10 at 16:10:36 UT. Right panels: Synthetic EOVSA microwave images generated from the combined MHD and particle model. Overlaid gray curves are magnetic field lines derived from the MHD model.

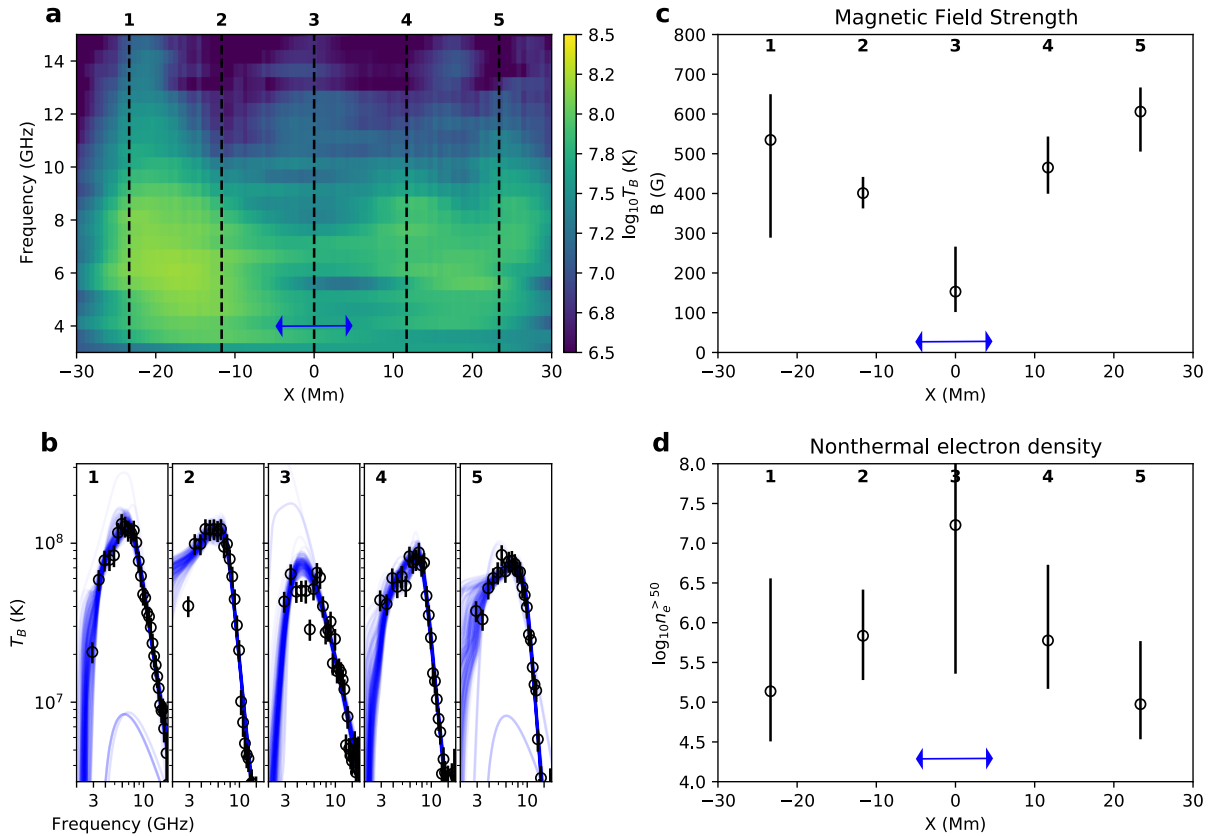


Figure 6. Spatially resolved microwave spectra and derived source parameters along the above-the-looptop, arcade-like microwave source. (a) Frequency–space spectrogram obtained along a fiducial slit drawn along the spine of the microwave source (white dashed curve in Figure 3(d)). (b) Example microwave brightness temperature spectra at five sampled locations along the slit (vertical dashed lines in (a) marked from 1 to 5). Black circles with error bars are the measurements, and blue curves are a subset of 200 randomly selected model spectra from the MCMC runs, each of which has a total of 800,000 samples. (c) and (d) Distribution of best-fit magnetic field strength B and total nonthermal electron density above 50 keV $n_e^{>50}$ along the slit. The double-side blue arrows mark the approximate location of the magnetic bottle region.

cusp-like shape after they pass the Y point. Then, the outflows quickly slow down until they join the flare

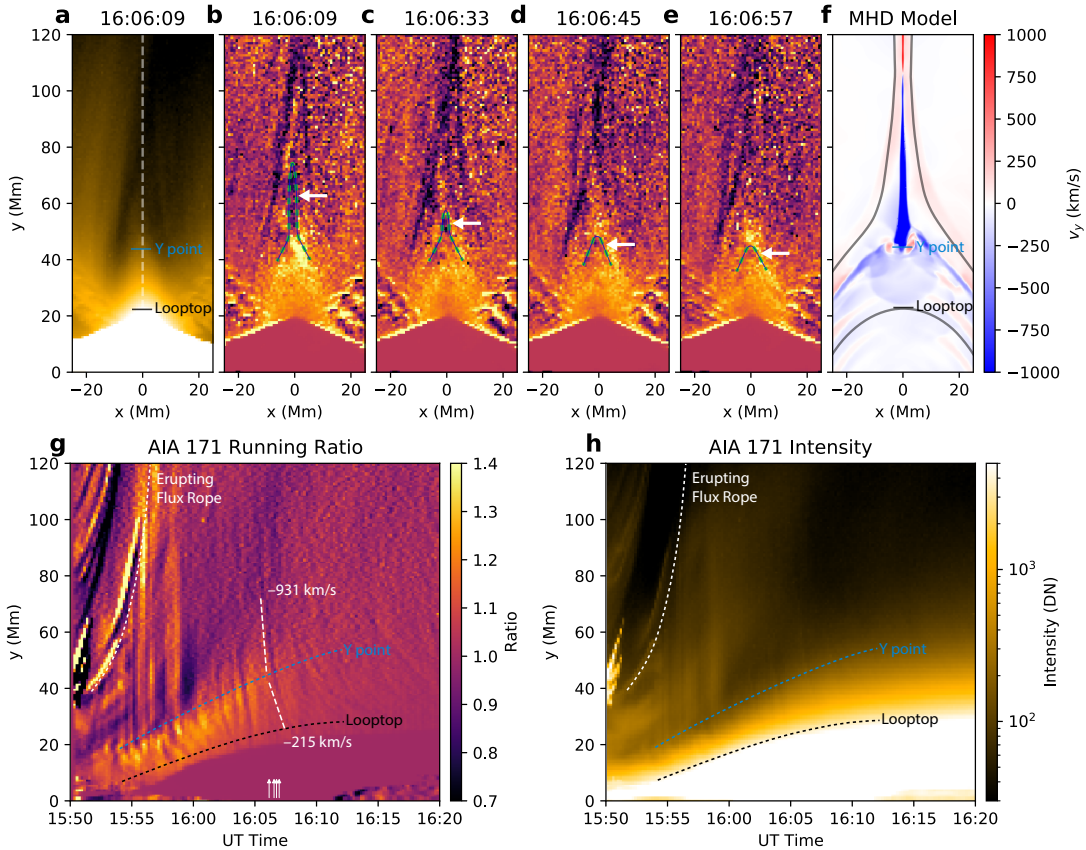


Figure 7. Plasma outflows slow down and transform to a cusp shape as they pass the magnetic bottle hosting the Y point. (a) Context SDO/AIA 171 Å EUV image at 16:06:09 UT. (b)–(e) Time-series of running-ratio SDO/AIA 171 Å images. Each plot shown is a ratio of the current image to a time 36-s earlier. The arrows indicate the downward plasma outflow that transforms from a linear shape to a cusp shape as it passes the Y point. (f) Corresponding MHD model showing the vertical component of the flow velocity. Downward plasma outflows (blue color) dominate the region above the Y point. (g) Time-distance plot of SDO/AIA 171 Å running-ratio time-series images obtained along a vertical slice at the central current sheet region (white dashed line in (a)). Approximate tracks of the bottom of the erupting flux rope, Y point, and looptop are marked as dashed curves. The example outflow event in (b)–(e) is marked by the two white dashed lines, which display an abrupt speed change after it passes the Y point. (h) Same as (g), but showing the original SDO/AIA 171 Å intensity.

arcade and relax to a potential state with a loop-like shape. This process is clearly shown in the SDO/AIA 171 Å EUV time-series images. In Figures 7(b)–(e), to better present the dynamic features, we plot a series of running-ratio images, each showing the intensity ratio of the current image to the one from 36-s earlier. There, a downward moving feature at the central current sheet location is seen to transform from an initially linear shape to a cusp shape as it moves across a location at $y \approx 43$ Mm. Such a transformation is already suggestive of the presence of a Y point at this location.

Furthermore, in Figure 7(g), we show a space-time diagram obtained at a vertical slice located at the central current sheet. Multiple downward-moving features can be distinguished as tracks that orient toward the lower-right direction. The example downflow event shown in panels (b)–(e) has an initial speed of >900 km s $^{-1}$ and

quickly slows down to only ≈ 200 km s $^{-1}$ after it passes the same location. Such a sudden slow-down motion of plasma downflows further supports the presence of the Y point. Coincidentally, the Y point identified with the EUV imaging observations alone matches almost exactly with the location of the ALT HXR source shown in Figure 3. It is also fully consistent with the location of the Y-point-hosting magnetic bottle structure inferred from the microwave spectral imaging analysis, which has a weaker magnetic field strength.

We note that the plane-of-sky-projected speed of the observed plasma downflow above the Y point (~ 900 km s $^{-1}$) seems slower than the inferred local Alfvén speed in the ALT magnetic bottle region ($v_A \approx 1,900$ km s $^{-1}$ for $B \approx 150$ G, constrained by our microwave spectral imaging analysis, and $n_{th} \approx 3 \times 10^{10}$ cm $^{-3}$, constrained by Hinode/EIS measure-

ments discussed in Appendix C. By combining line-of-sight (LOS) flow measurements made by Hinode/EIS and plane-of-sky measurements from SDO/AIA, French et al. (2024) reported that despite that the reconnection current sheet appears to be viewed perfectly edge-on, the non-zero LOS speeds in the downflow region suggest that the current sheet is tilted slightly away from the observer. Therefore, the physical flow speed should be greater than that measured in the plane of the sky, although the required projection correction is likely insignificant given the low LOS speed ($<35 \text{ km s}^{-1}$) measured by Hinode/EIS. Moreover, it has been shown in recent 3D modeling that the speed of the observed plasma outflows in EUV time-series images may be substantially slower than the intrinsic reconnection outflows (Shen et al. 2023). Lastly, as argued by Chen et al. (2020b), the low cadence of SDO/AIA (12 s) may simply render flows faster than $\sim 2,000 \text{ km s}^{-1}$ undetectable within the flaring region because they would traverse a large distance of $>50 \text{ Mm}$ in two frames. For these reasons, we argue that super-magnetosonic outflows may still be present to drive a fast-mode termination shock in the magnetic bottle region to facilitate the acceleration of the energetic particles.

3. MHD, PARTICLE, AND EMISSION MODELING

The multi-wavelength analysis above suggests that the ALT magnetic bottle region is where the majority of the microwave- and X-ray-emitting nonthermal electrons are concentrated. To further elucidate the role of the magnetic bottle and the underlying physical processes, we combine a data-informed macroscopic MHD and particle model to simulate the acceleration and transport of energetic electrons in a realistic flare geometry. The resistive 2.5-D MHD simulation we perform here is similar to those used in our earlier works (Chen et al. 2015, 2019; Shen et al. 2018), which features a dynamic fast-mode termination shock in the ALT magnetic bottle region. Appropriate scaling is applied to the MHD model to adjust to the observed flare size and observational constraints of the plasma properties. To model the electron acceleration and transport processes in the macroscopic flare geometry, we adopt the method used in Kong et al. (2019) by injecting pseudo electrons into the MHD model and simulating their kinetic evolution by solving the Parker transport equation. In the model, the electrons are found to be primarily accelerated via the Fermi mechanism due to compression (Fermi 1949; Parker 1965) in the magnetic bottle region, where the downward plasma flows collide head-on with the newly reconnected field lines. The fast-mode termination shock further facilitates the acceleration thanks

to the sharp jump of physical parameters across the shock surface (Kong et al. 2019). We refer interested readers to Appendix Section C and references therein for more technical details.

The combined MHD and particle model results in spatially, temporally, and spectrally resolved nonthermal electron and thermal plasma distribution in the simulation domain. Figures 8(a) and (b) show the distribution of $>50 \text{ keV}$ and $>300 \text{ keV}$ nonthermal electrons, respectively, with example electron spectra derived from three different locations in the model shown in Figure 8(c). After scaling the dimensionless electron distribution in the model with physical units constrained by the observations, similar to the microwave and HXR analysis results, the distribution of $>50 \text{ keV}$ electrons peaks in the magnetic bottle region with a number density of $5 \times 10^6 \text{ cm}^{-3}$ and drops rapidly to $<1\%$ of the peak value beyond $|x| > 20 \text{ Mm}$ (see contours in Figure 8(d)).

By combining the resulting distribution of energetic electrons from the particle model $dn_e/d\varepsilon(x, y, \varepsilon)$ and plasma properties including magnetic field $B(x, y)$, thermal plasma density $n_{\text{th}}(x, y)$, and temperature $T(x, y)$ from the MHD model, we generate synthetic SDO/AIA EUV, RHESSI HXR, and EOVSAs microwave images at different energy/frequency bands. Appropriate emission mechanisms are assumed for each emission type: optically thin line emissions for EUV, thin-target bremsstrahlung for HXRs, and nonthermal gyrosynchrotron emission for microwaves. The corresponding instrument response is also considered (see Appendix Section D for details). Figure 8(e) shows a composite of the resulting synthetic SDO/AIA 131 Å EUV image (background), RHESSI 25–60 keV HXR image (red contours), and multi-frequency EOVSAs microwave images (filled color contours). All of the images display a striking resemblance to the observations shown in Figure 8(f): The EUV 131 Å image displays a bright, closed arcade with a cusp-shaped top. A compact HXR source is located in the magnetic bottle region near the fast-mode termination shock above the flare arcade. Meanwhile, similar to the observations, the multi-frequency microwave source resembles an arcade-like shape at the outer rim of the flare arcade. Figure 5 shows a side-by-side comparison between the observed and modeled microwave images at the same frequencies. Figures 8(e) and (f) display another comparison with the microwave images shown as overlaying filled contours colored from red to blue for increasing frequencies. One can see the model images resemble the observed ones remarkably well. Moreover, as shown in Figure 9, not only does the modeled microwave source morphology achieve an excellent match with the observations, but the spatially

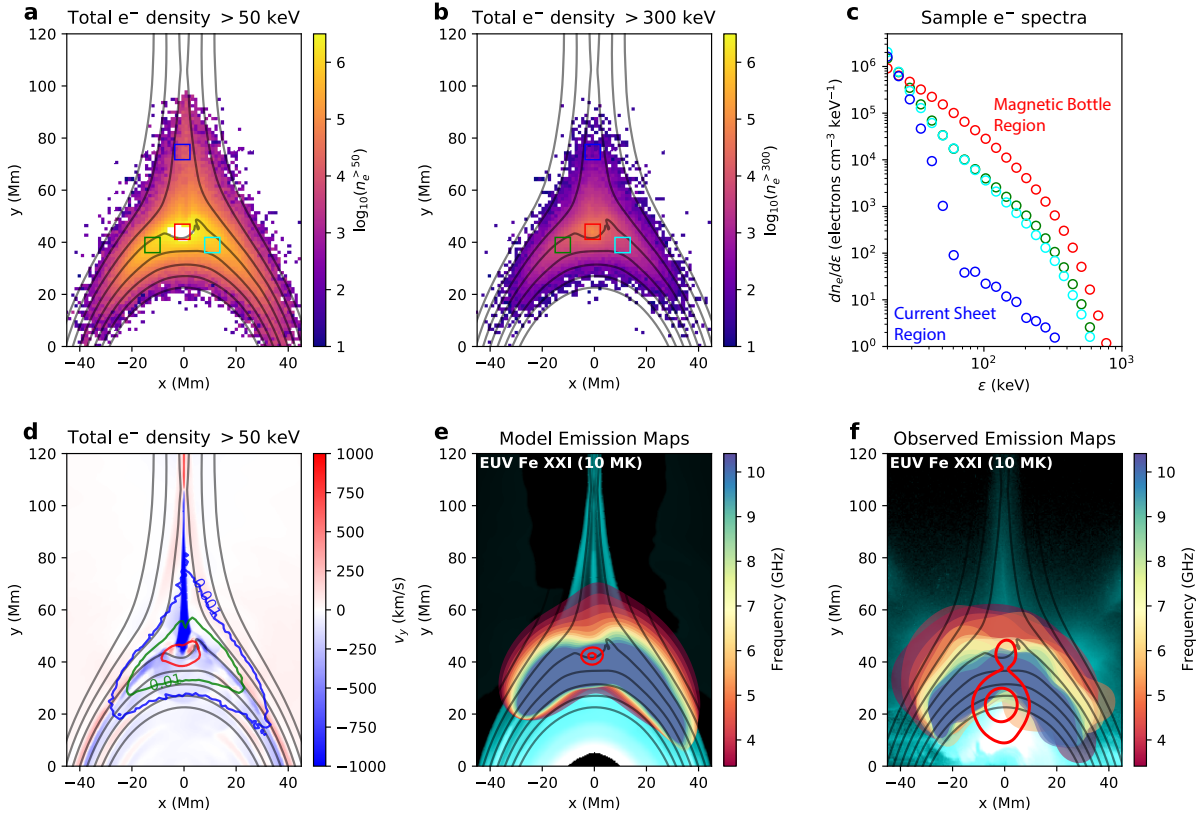


Figure 8. Distribution of nonthermal electrons around the magnetic bottle region and the associated emissions. (a) and (b) Spatial distribution of > 50 keV and > 300 keV electrons, respectively. Note they are shown on a logarithmic scale. (c) Example model nonthermal electron spectra from four regions marked in panels (a) and (b), with one located near the Y point (red), two in the loop legs (green and cyan), and one in the current sheet region (blue). (d) Contours of > 50 keV electron distribution overlaid on the model v_y map. Blue, green, and red contours are 0.1%, 1%, and 15% of the peak electron density, respectively. In particular, the innermost red contour encloses 51% of all the > 50 keV electrons. (e) Synthetic SDO/AIA (background), 25–60 keV HXR (red contours), and multi-frequency microwave sources (filled color contours) as calculated from the combined MHD and particle model. (d) Multi-frequency observations identical to Figure 3(d), overlaid with magnetic field lines derived from the model.

resolved microwave spectra derived from different regions also yield a qualitative agreement, demonstrating the success of our approach. The microwave source’s appearance is very different from its HXR counterpart mainly because, unlike the X-ray bremsstrahlung, gyrosynchrotron radiation has a strong dependence on the local magnetic field.

Intriguingly, unlike the HXR source that is highly localized at the ALT magnetic bottle, similar to the observations, the multi-frequency microwave source extends well beyond the region toward the directions of the current sheet and the two footpoints. Such a large extension suggests that, while the majority of the energetic electrons are confined within the ALT HXR source near the Y point—in the model, it contains $\sim 50\%$ of the total > 50 keV electrons (see red contour in Figure 8(d))—a small fraction of these electrons manage to escape and

spread beyond the magnetic bottle region (albeit “diluted” to a much smaller density), giving rise to the extended microwave source with an arcade-like shape.

We note that in the observations, another strong loop-top X-ray source is present, whose centroid is located at $y \approx 24$ Mm (Figure 8(f)). Spectral analysis results suggest that it is extremely hot (15–27 MK) and dense (up to 10^{12} cm^{-3}). This source has been interpreted as the result of thermalization of previously accelerated nonthermal particles (Veronig & Brown 2004), colliding chromospheric upflows (Reeves et al. 2007), or compression by slow shocks formed by sheared reconnection (Longcope & Guidoni 2011). Reproducing this additional source in a model requires the inclusion of feedback between the thermal plasma and nonthermal particles, more accurate treatment of the chromospheric evaporation processes, and modeling of the reconnect-

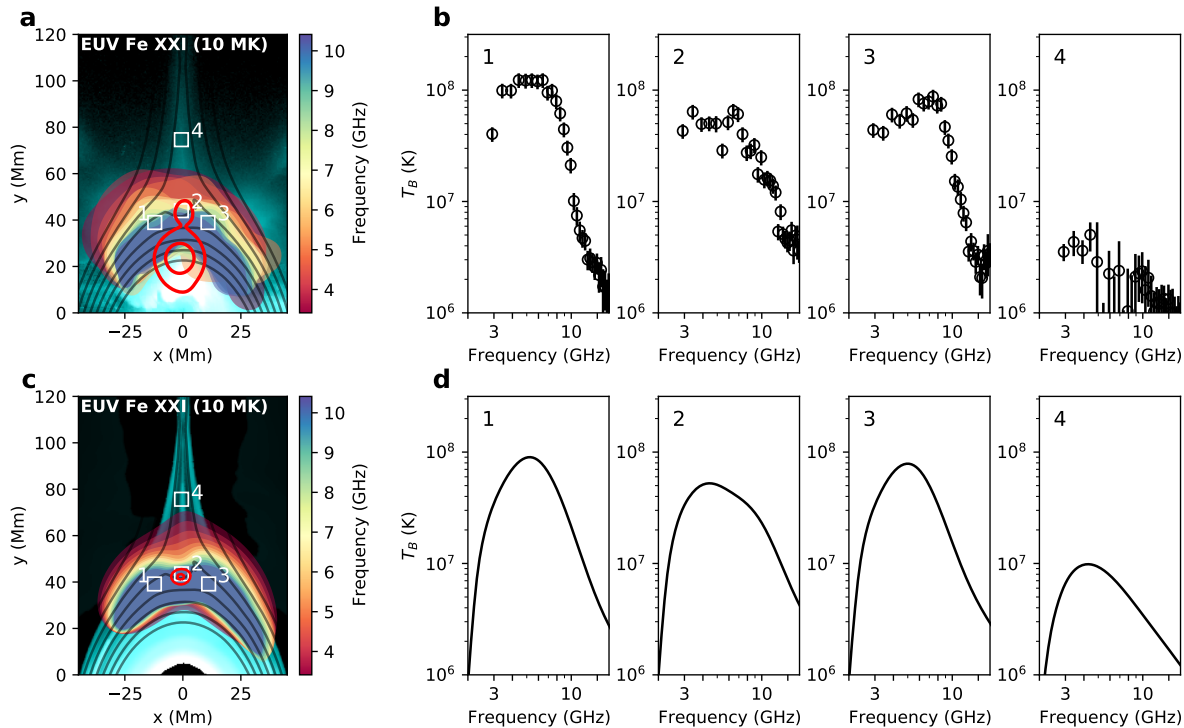


Figure 9. Comparison between the observed and modeled microwave images and spectra. (a) Observed multi-frequency microwave images overlaid on SDO/AIA 131 Å EUV image (identical to Figure 8(f)). (b) Sample microwave spectra derived from four selected regions marked in (a). (c) and (d) are identical to (a) and (b), but instead showing the modeled multi-frequency microwave images and the corresponding sample spectra.

tion processes in the third dimension, which is beyond the scope of our current work.

4. DISCUSSION AND CONCLUSION

We have demonstrated that our model, which includes both MHD and particle processes in a realistic flare geometry, can reproduce emission signatures that are well-matched to multi-wavelength observations. In the model, the energetic electrons are found to be primarily accelerated in the magnetic bottle region by the converging flows and facilitated by the fast-mode termination shock via the Fermi mechanism. The accelerated electrons are further trapped there due to pitch-angle scattering by turbulence. This is the first time when synthetic observables in both the thermal and nonthermal regimes are generated from a self-consistent, macroscopic numerical model to compare with microwave, EUV, and X-ray imaging and spectroscopy observations. Such a remarkable agreement between the modeled and observed emissions suggests that this model of electron acceleration and transport is a viable approach during this period of interest.

The presence of the magnetic bottle structure in the above-the-looptop region of this event is well supported by its lower magnetic field strength derived from the mi-

crowave imaging spectroscopy data (Figure 6), as well as the observed abrupt change in the morphology and speed of the EUV plasma downflows (Figure 7). Direct evidence for fast-mode termination shocks is more elusive due to various challenges in identifying them observationally (see, e.g., discussions in Chen et al. 2019). However, recently, new and convincing evidence for their existence started to emerge. For this particular event, by using EUV imaging spectroscopy data recorded by Hinode/EIS, French et al. (2024) reported a sharp gradient in the Doppler velocity of hot (~ 18 MK) EUV downflows in the above-the-looptop region. The location and characteristics of the sharp velocity gradient agree very well with an MHD model that features a fast-mode termination shock at the same location. In addition, Cai et al. (2019) argued that the hot “supra-arcade fan” structure, observed by SDO/AIA, Hinode/EIS, and the Interface Region Imaging Spectrograph (IRIS), was possibly caused by a termination shock, albeit that the reported structure is not located above the main flaring arcade, but a loop system south of that.

The escaped nonthermal electrons from the above-the-looptop region gyrate in the magnetic field and produce microwave sources that form an arcade-like shape striding *above* the bright EUV flare arcade. The ab-

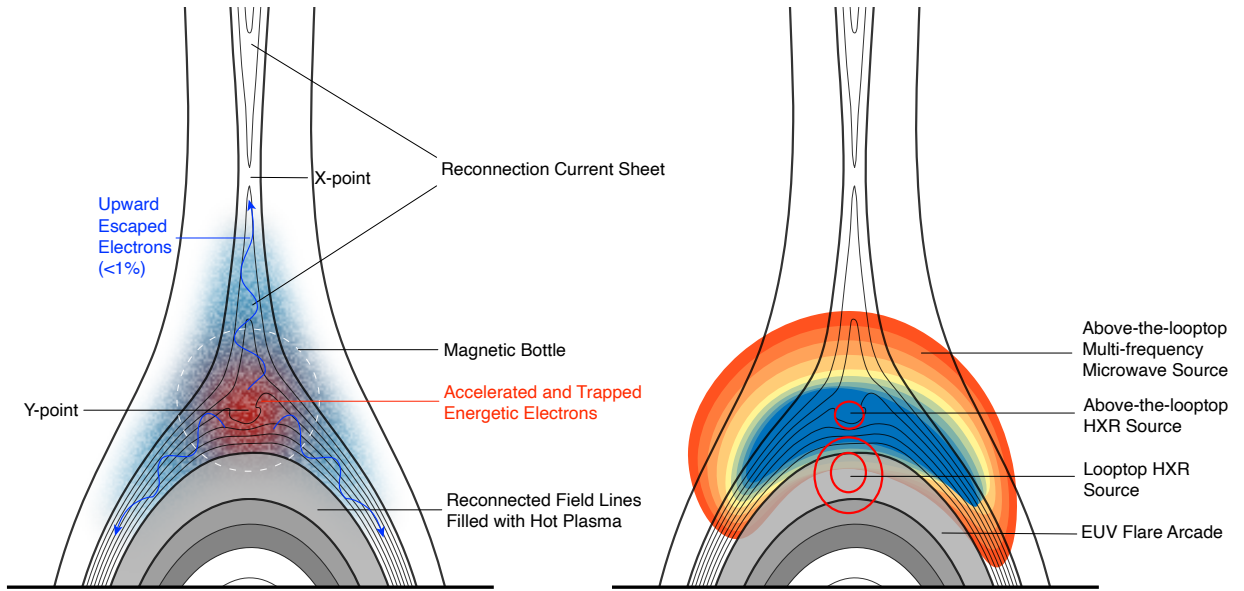


Figure 10. Physical picture suggested by our combined observation-modeling results. Energetic electrons are accelerated via the Fermi mechanism and trapped in the above-the-looptop magnetic bottle region due to turbulence. The reconnected and relaxed magnetic loops filled with hot plasma are observed as a bright EUV flare arcade with a hot looptop HXR source. The highly concentrated energetic electrons near the Y point produce the above-the-looptop HXR source via bremsstrahlung. Meanwhile, a small fraction of energetic electrons escaping from the magnetic bottle region produces the observed multi-frequency microwave source with a large extension, which has an arcade-like shape bestriding above the EUV flare arcade.

sence of an HXR footpoint source in our case suggests that it is either partially occulted by the solar limb at the time or the flux of nonthermal electrons reaching the footpoints is insufficient to produce observable HXR footpoint emission in the presence of a bright looptop source. In other cases when HXR footpoint sources are co-observed, they are often found to be located at the outer edge of bright EUV flare arcades (e.g., Liu 2013; Krucker & Battaglia 2014). These observations nicely corroborate our scenario: they result from accelerated nonthermal electrons escaping from the ALT magnetic bottle region and reaching the footpoints along the freshly reconnected field lines (see, e.g., recent modeling results by Kong et al. 2022b).

As depicted in Figure 10, most of the accelerated electrons are confined near the Y point, producing the observed ALT HXR source. Meanwhile, the full extension of the observed microwave source traces 0.1–1% of the peak >50 keV nonthermal electron density, or merely a millionth of the background plasma density! Our observations demonstrate the extreme sensitivity of microwave emission to even a tiny population of flare-accelerated nonthermal electrons. Such a sensitivity is partially benefited from the Razin effect (Ginzburg & Syrovatskii 1965). This effect strongly suppresses the microwave brightness in regions with relatively low magnetic field strength and high thermal plasma density,

which are the exact features of the magnetic bottle region in our case. Strong Razin suppression occurs below a critical frequency of $\nu_c \approx 20n_{\text{th}}/B$, or $\approx 5\text{--}6$ GHz in the magnetic bottle region. This suppression effect is likely responsible for the apparent “gap” in the observed and modeled microwave sources at around $x = 0$ Mm for frequencies $\lesssim 6$ GHz (see Figure 5). Also, it effectively reduces the microwave brightness of the magnetic bottle region despite its high concentration of nonthermal electrons and, in turn, facilitates the detection of microwave sources arising from an extremely small nonthermal electron population outside the region.

The strong concentration of nonthermal electrons within the magnetic bottle region has important implications for electron acceleration and transport processes. First, it is highly likely that the nonthermal electrons are primarily accelerated in the magnetic bottle region itself rather than injected from elsewhere, such as high up in the reconnection current sheet or low in the loop legs. As shown in Figure 8(d), our joint observation–modeling results suggest that the nonthermal electron density rapidly drops to $<1\%$ of the peak value outside the ALT magnetic bottle region in all directions. Such a large density contrast implies that if the injection-and-trapping process is responsible, it must be a slow process. For instance, assuming all the electrons are injected from the upper current sheet, pure

injection of 50 keV electrons without any loss takes $\tau^{\text{inj}} \approx N_e^{\text{ALT}}/F_e^{\text{inj}} = n_e^{\text{ALT}}L_y^{\text{ALT}}A_{xz}^{\text{ALT}}/(n_e^{\text{CS}}v^{\text{inj}}A_{xz}^{\text{CS}}) \approx (n_e^{\text{ALT}}/n_e^{\text{CS}})(A_{xz}^{\text{ALT}}/A_{xz}^{\text{CS}})L_y^{\text{ALT}}/v^{\text{inj}}$, where $n_e^{\text{ALT}}/n_e^{\text{CS}} > 100$ is the ratio of the nonthermal electron density between the ALT and current sheet region, $A_{xz}^{\text{ALT}}/A_{xz}^{\text{CS}} > 50$ is the expansion factor of the cross-section between the magnetic bottle region (with a width of $L_x^{\text{ALT}} \approx 10$ Mm) and the narrow current sheet (with a width of $L_x^{\text{CS}} \approx 0.2$ Mm, the grid size of the numerical model), L_y^{ALT} is the vertical extension of the ALT region taken to be ~ 5 Mm as suggested in the model, and v^{inj} is the injection speed of the electrons, taken the kinetic speed of 50 keV electrons $v_e^{50} \approx 0.41c$ as the upper limit. The estimated injection timescale to produce the ALT source is $\tau_{\text{inj}} > 200$ s, even without any loss. This timescale is much longer than the typical acceleration timescale inferred from HXR and radio emissions, which can display rapid fluctuations at second or even subsecond scales (e.g., Fletcher et al. 2011 and references therein), although we note that the acceleration in the flare gradual phase may be less variable and, as such, may have an inherently longer timescale. While we cannot entirely rule out such an injection-and-trapping scenario owing to the insufficient observational constraints for the precise dimensions of the ALT region (particularly in the line-of-sight z direction), we conclude that local acceleration and trapping in this region is a more likely scenario to account for the profound concentration of the nonthermal electrons in the ALT magnetic bottle region.

Second, such a concentration requires effective trapping of the energetic electrons. In our model, we invoke diffusion in the strong pitch-angle scattering regime induced by turbulence with a prescribed Kolmogorov-type spectrum. In this case, pitch-angle diffusion quickly leads to an isotropization of the electron distribution, and the transport processes can be approximated by Parker’s transport equation. Although our model yields a good match with the observations after adjusting for the (essentially unknown) diffusion parameters, it is certainly not a unique approach. For example, other analytical and numerical models for the trapping-and-precipitation processes can be found in the literature, some of which involve treatments for the diffusion processes due to both momentum and pitch-angle scattering as well as collisional loss (Chen & Petrosian 2013; Kontar et al. 2014; Kong et al. 2022b).

Finally, our results provide new insights into understanding the puzzling departure from equipartition between the upward-escaped and downward-retained energetic electron population reported by studies that combine remote-sensing and *in situ* observations, which have concluded consistently that only 0.1–1% of the flare-

accelerated energetic electrons manage to escape to interplanetary space (Lin 1974; Krucker et al. 2007; Wang et al. 2021, 2023a). Such a large imbalance not only poses a challenge for understanding the particle acceleration and transport processes, but also has important implications for space weather in solar and extrasolar systems. In our scenario, this imbalance naturally occurs because the primary acceleration site is the magnetic bottle located *below* the X point, with the newly reconnected, cusp-shaped field lines in the large-scale current sheet acting as a nearly closed structure to limit the upward-directed electrons from escaping (Figure 10). Along with efficient trapping, as in our case, the energetic electron density reaching the X point can be only $<1\%$ of that at the core acceleration region, giving rise to an extremely small fraction of these energetic electrons that enter interplanetary space.

We note that, however, since our model does not involve an exhaustive search in the parameter space and does not include all possible particle energization/transport mechanisms, it is by no means exclusive. Other scenarios that result in an efficient energization and confinement of nonthermal electrons in the magnetic bottle region while allowing only a small fraction of them to escape may also be possible. Some candidates may include magnetic islands (Drake et al. 2006; Guidoni et al. 2022), collapsing traps (Somov & Kosugi 1997), and intense shock heating (Masuda et al. 1994; Mann et al. 2024), yet rigorous data–model comparisons are required to further examine these models. Moreover, in order to achieve a more definitive understanding, extensive studies are needed for a large sample of flare events with different intensities and geometries. Last but not least, to make further progress, next-generation telescopes capable of performing radio and HXR imaging spectroscopy with orders of magnitude higher dynamic range and sensitivity, as well as more sophisticated models are desired. Notable future telescope concepts include the Frequency Agile Solar Radiotelescope (FASR; Gary et al. 2023 and Chen et al. 2023) in radio wavelengths and the Focusing Optics X-ray Solar Imager (FOXSI; Christe et al. 2016) or its variants (e.g., COMPLETE; Caspi et al. 2023) in X-rays.

ACKNOWLEDGMENTS

This work is primarily funded by NASA Heliophysics Supporting Research grant 80NSSC20K1318 to NJIT, SAO, UMN, and LANL. B.C. and S.Y. receive additional support from NSF grants AST-1735405 and AST-2108853 to NJIT. The authors are grateful to Dr. Harry Warren for providing the Hinode/EIS temperature and emission measure maps. They also thank Drs. Alexey Kuznetsov and Gregory Fleishman for making their fast gyrosynchrotron codes available. X.K. is supported by NSFC grants 42074203 and 11873036. C.S. is supported by NASA grants 80NSSC19K0853, 80NSSC21K2044, and NSF AST 2108438 to SAO. X.L. acknowledges the support from NASA through grant 80NSSC21K1313, NSF grant AST-2107745, SAO through subcontract SV1-21012, and LANL through subcontract No. 622828. The Expanded Owens Valley Solar Array (EOVSA) was designed and built and is now operated by the New Jersey Institute of Technology (NJIT) as a community facility. EOVSA operations are supported by NSF grant AGS-2130832 and NASA grant 80NSSC20K0026 to NJIT. The authors are grateful to the RHESSI, SDO, SOHO/LASCO, and GOES-R/SUVI teams for making their data publicly available.

Facilities: OVRO:SA, RHESSI, SDO, Hinode, SOHO, GOES

APPENDIX

A. X-RAY DATA ANALYSIS

RHESSI observed the event with its detectors 1, 3, 6, and 8. During the time of interest, the attenuator state was set to A3, meaning both the thin and thick attenuators were used. X-ray imaging is performed using measurements made by detectors 3, 6, and 8 with the CLEAN algorithm (Hurford et al. 2002). The nominal angular resolution of the finest grid used for imaging (detector 3) is $6''.8$, which is used as the FWHM width of the synthesized beam for restoring the CLEAN images. Figure 11 shows the resulting X-ray images integrated between 16:10:00 UT and 16:11:10 UT in 10–16 keV, 16–25 keV, and 25–60 keV.

X-ray spectral analysis is performed using the `ospex` software (Schwartz et al. 2002). We use the data from detector 3 (which had the lowest sensitivity at the time and hence was less affected by the pile-up effect) to obtain the X-ray count flux spectrum between 16:10:00 UT and 16:11:08 UT. The resulting X-ray photon flux spectrum after applying the instrument response matrix is shown in Figure 4 as black curves. Spectral modeling is performed in the 12–60 keV range using two isothermal functions and one nonthermal bremsstrahlung model. Also included in the spectral modeling is the pile-up module. We performed spectral analysis assuming both the thick- and thin-target regimes. In both regimes, the thermal components, which dominate the spectrum below ~ 30 keV, include a hot ~ 15 MK looptop source with a volume emission measure of $\approx 2 \times 10^{51} \text{ cm}^{-3}$. A secondary superhot component with a temperature of 27–28 MK and a volume emission measure of $\approx 4 \times 10^{49} \text{ cm}^{-3}$ is also present. Assuming a source volume $V \approx (10 \text{ Mm})^3$ according to the size of the source shown in the X-ray image, the plasma density for the two thermal components becomes $\approx 1 \times 10^{12} \text{ cm}^{-3}$ and $2 \times 10^{11} \text{ cm}^{-3}$, respectively. Such a high density associated with the hot 15 MK component is sufficient to stop all nonthermal electrons up to 70 keV in the source (with a half-width of ~ 5 Mm) through Coulomb collisions (Tandberg-Hanssen & Emslie 1988).

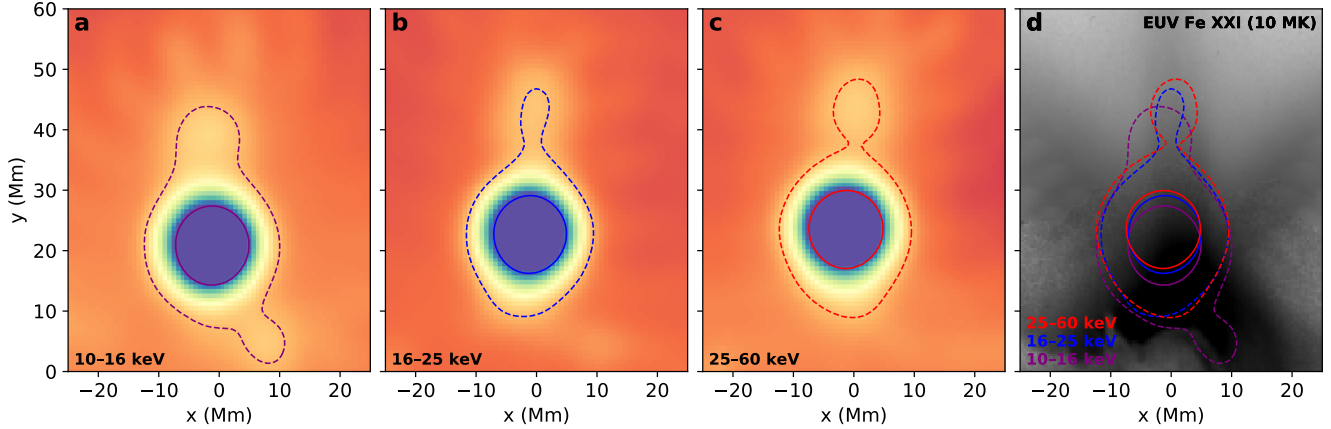


Figure 11. RHESSI X-ray images for the time of interest on 2017 September 10. The time interval used for imaging is 16:10:00-16:11:10 UT. The energy ranges used for imaging are 10–16 keV, 16–25 keV, and 25–60 keV, shown in panels (a), (b), and (c) respectively. The solid and dashed lines denote the 50% and 10% contours. Panel (d) shows X-ray images of all three energy ranges overlaid on SDO/AIA 131 Å (Fe XXI) EUV image at the closest time (shown in reversed gray-scale).

For the nonthermal component, if the component falls into the thick-target bremsstrahlung regime due to interactions with an extremely dense plasma environment, such as the looptop X-ray source with a density of $n_{\text{th}} > 10^{12} \text{ cm}^{-3}$, the best-fit yields a nonthermal electron distribution with a total electron flux of $F_e^{>50} \approx 5 \times 10^{33} \text{ electrons s}^{-1}$ above 50 keV and a power-law index of the electron flux spectrum $\delta^{\text{thick}} \approx 5.3$. However, if the component is instead associated with thin-target bremsstrahlung in a relatively tenuous coronal plasma environment, such as the ALT region with a density of $n_{\text{th}} \approx 3 \times 10^{10} \text{ cm}^{-3}$, the fit returns a normalization factor of $n_{\text{th}} V f_e^{>50} = n_{\text{th}} L_z F_e^{>50} = 1.6 \times 10^{54} \text{ cm}^{-2} \text{ s}^{-1}$ with a power-law index of $\delta^{\text{thin}} = 4.7$, where L_z is the source column depth, $f_e^{>50} = \int v_e(\varepsilon) \frac{dn_e}{d\varepsilon} d\varepsilon$ is the total electron flux density above 50 keV, and $F_e^{>50} = f_e^{>50} A$ is the total >50 keV electron flux in a source cross-section of A . Taking a background plasma density of $n_{\text{th}} \approx 3 \times 10^{10} \text{ cm}^{-3}$ and a source column depth of $L_z \approx 10 \text{ Mm}$, the nonthermal electron flux above 50 keV is one order of magnitude greater than the thick-target case, at $F_e^{>50} \approx 5 \times 10^{34} \text{ electrons s}^{-1}$. The corresponding total nonthermal electron density above 50 keV is $n_e^{>50} \approx F_e^{>50} / (v_e^{50} A) \approx 4 \times 10^6 \text{ cm}^{-3}$. We find the parameters returned from the thin-target regime may yield a better agreement with the microwave analysis results.

As RHESSI was approaching the end of its operations at the time of the observation, only 4 of the 9 detectors operated nominally, which limited its imaging capabilities. Furthermore, SOL2017-09-10 was one of the brightest flares ever observed by RHESSI. Despite that both attenuators were inserted, the count rate nevertheless stayed high, and pileup effects occurred (i.e., two photons arrive essentially simultaneous, and they are therefore measured as a single photon with the summed energy of the two individual photons). While the time used for the analysis is ~ 12 minutes past the flare peak, which has lessened the pileup issue, and pileup correction following the standard procedure has been applied in our fitting, the spectral analysis is possibly still pushing to the limits of the instrumentation. Hence, despite the fact that the spectral fitting results are consistent with other complementary data, we suggest that they should be considered with some level of caution. For imaging, pileup correction is not available, making the exact partition of the X-ray photons between the looptop and ALT X-ray source undetermined. However, as pileup only affects imaging by removing a rather small fraction of photons as they pile up and appear at higher energies, the imaging morphology is not much affected for energies below ~ 36 keV (two times the peak of the count spectrum at ~ 18 keV). We therefore conclude that the double-source structure seen in the X-ray images is trustworthy. However, we can not draw any firm conclusion on the true shape and brightness of the ALT X-ray source.

B. MICROWAVE DATA ANALYSIS

EOVSA observed the SOL2017-09-10 X8.2 flare event in the range 2.5–18 GHz with 31 evenly spaced spectral windows, each of which has a bandwidth of 160 MHz. The center frequencies of these spectral windows are $\nu = 2.92 + 0.5n$ GHz, where n is the spectral window number from 0 to 30. Different from Chen et al. (2020b) and Fleishman et al. (2022), which analyzed the earlier and main impulsive phase of the event, respectively, the time of interest for this study is around 16:10 UT during the gradual phase of the flare when the magnetic flux rope has already

propagated to a large distance, allowing detailed observation–modeling comparison. Methods used for calibrating and imaging the EOVSA data are identical to our earlier studies (see Gary et al. 2018 and Chen et al. 2020b). The integration time used for synthesis imaging is 4 s, and a circular beam with an FWHM size of $10''.2/[\nu/10 \text{ GHz}]$ is used to restore the final microwave images after deconvolution. Figure 5 shows an example of multi-frequency EOVSA images from 3.4 GHz ($n = 1$) to 10.4 GHz ($n = 15$) at 16:10:36 UT.

Each spatially resolved microwave spectrum used for spectral analysis is derived from the average brightness temperature in an $8'' \times 8''$ area (corresponds to the resolution at ~ 12.4 GHz). For each spatially resolved spectrum, a power-law nonthermal electron distribution $dn_e(\varepsilon)/d\varepsilon$ with a spectral index of δ' and total nonthermal density $n_{\text{nth}}^{>50}$ above 50 keV is used to model the spectrum based on the fast gyrosynchrotron codes (Fleishman & Kuznetsov 2010). Other model parameters used in the fit include the magnetic field strength B , thermal plasma density n_{th} of the source, and the viewing angle θ with respect to the magnetic field direction. The low- and high-energy cutoff of the electron distribution ε_{min} , ε_{max} , and the plasma temperature are fixed to 25 keV, 10 MeV, and 15 MK, respectively. For the Markov chain Monte Carlo analysis, similar to Chen et al. (2020b), we use a logarithmic likelihood function in the following form:

$$\ln p = -\frac{1}{2} \sum_n \left[(T_{b,i}^o - T_{b,i}^m)^2 / \sigma_{T_{b,i}}^2 + \ln(2\pi\sigma_{T_{b,i}}^2) \right], \quad (\text{B1})$$

where $T_{b,i}^o$ and $T_{b,i}^m$ are the observed and modeled brightness temperature at frequency ν_i , respectively, and $\sigma_{T_{b,i}}$ is the corresponding uncertainty estimated by adding the r.m.s. brightness temperature of a region in the image without any sources and a fractional error in the source brightness temperature (assumed to be 15%) in quadrature. We then use `emcee` (Foreman-Mackey et al. 2013), a Python implementation of the affine-invariant MCMC ensemble sampler (Goodman & Weare 2010), to sample the parameter space according to the likelihood function. The multi-parameter posterior distribution allows us to find the best-fit model parameter values, taken as the median value of the samples in each marginalized distribution (i.e., the 50% percentile). The lower and upper $1\text{-}\sigma$ uncertainties are taken as the 16% and 84% percentile of the samples in each distribution, respectively. For the MCMC analysis of each spectrum, we use 100 “walkers” to sample the parameter space, each of which draws a total of 8000 samples.

C. MHD AND PARTICLE MODELING

The setup of the MHD model follows similar procedures as those described in Shen et al. (2018) but with a different scaling to better match the observations of the particular event of interest. The initial setup is a Harris-type vertical current sheet centered at $x = 0$ that separates two regions of the magnetic field with opposite polarity, which are line-tied at the lower boundary. A guide field of $B_g = 0.1B_0$ is introduced (where B_0 is the normalized magnetic field), and the initial background plasma beta is set to $\beta_0 = 0.01$. The magnetic field lines are line-tied to the bottom boundary and are open at the top boundary. Reconnection proceeds in the current sheet and forms a series of post-flare arcades. Above the looptop, reconnection continues in the current sheet, driving the flare evolution and plasma dynamics. For thermodynamic treatment, classical Spitzer thermal conduction is used. In this study, we focus on a period in the MHD simulation (96.5–97.5 t_0 in Shen et al. 2018) when the reconnection outflow is mostly laminar (i.e., without plasmoids), and the associated fast-mode termination shock is well-defined and nearly symmetric.

Since the MHD simulation is performed in dimensionless units, we can scale the model parameters to those constrained by our observations. In particular, the spatial scaling is done by comparing the sizes of the flare arcade and plasma sheet to the observations. The magnetic field scaling is informed by the microwave spectral diagnostics described in the “Microwave data analysis” section. Scaling of the thermal plasma density and temperature is mainly based on Hinode/EIS measurements of the flare arcade and plasma sheet regions with EUV imaging spectroscopy (see Warren et al. 2018 for details). Figure 12 shows distributions of plasma parameters in the MHD model at 97.4 t_0 , which include plasma density (panel (e)), temperature (panel (f)), magnetic field strength (panel (g)), and the vertical component of the plasma velocity (panel (h)). In comparison, we also show the plasma density and temperature maps derived from Hinode/EIS measurements of the Fe XXIV line pairs in panels (a) and (b)¹, as well as the Hinode/EIS Fe XXIV and SDO/AIA 131 Å (Fe XXI) intensity maps in panels (c) and (d). Magnetic field lines derived from the same MHD model are overlaid in all panels. It can be seen that the MHD model and the multi-wavelength observations yield a qualitative match in the flare geometry and various plasma properties. We note that both the Hinode/EIS and

¹ Hinode/EIS analysis returns emission measure. A uniform column depth of 10 Mm is assumed to estimate the plasma density in the flaring region.

SDO/AIA maps are affected by saturation at the brightest portion of the flare arcade (red dashed contour). Also, the maps show a diffraction pattern (with an “X” shape) originating from the brightest region. One should disregard the plasma diagnostics results from these regions corrupted by such effects.

The particle modeling adopts the method described in Kong et al. (2019). Similar approaches have been performed in several following studies (Kong et al. 2020, 2022b,a; Li et al. 2022). We refer interested readers to these works for more detailed descriptions. Briefly, mono-energetic electrons of an initial energy of 20 keV are injected into the MHD model as pseudo particles with an isotropic angular distribution. The kinetic evolution of these particles in the simulation domain is modeled by solving the Parker transport equation, which takes the fluid velocity and magnetic field input from the MHD model. Particle transport in the magnetic field is mainly modulated by stochastic diffusion by well-developed turbulence with a Kolmogorov-type power spectrum. The construction of the diffusion coefficient follows the treatment in Giacalone & Jokipii (1999), with the perpendicular diffusion assumed to be 10% of the parallel diffusion. The simulation domain has an area of 102.0 Mm \times 127.5 Mm with a uniform grid size of 0.22 Mm. The output of the model, binned to a grid size of 1.275 Mm, is a spatial distribution of nonthermal electrons at different energies. In the model, the electron momentum is distributed evenly in logarithmic space, with a total of 40 samples between 20 keV and 5450 keV.

Figures 12(i)–(l) shows the distribution of nonthermal electrons at four selected energies (50 keV, 100 keV, 200 keV, and 500 keV) from the particle model. Similar to the results in Kong et al. (2019), the nonthermal electrons

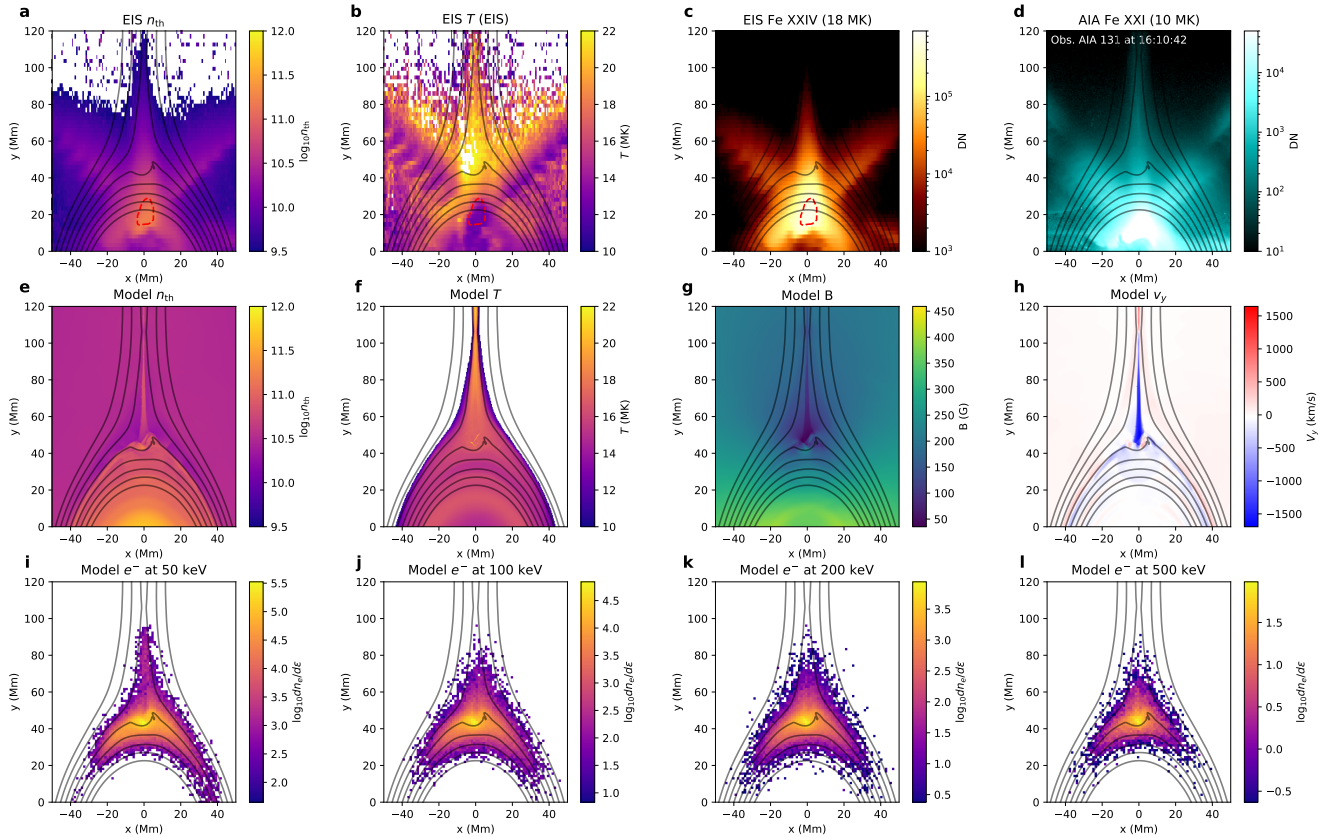


Figure 12. Data-informed MHD and particle modeling of the 2017 September 10 flare during its gradual phase at 16:10 UT. (a) and (b) Plasma density and temperature maps derived from Hinode/EIS measurements of the Fe XXIV line pairs. (c) and (d) Hinode/EIS Fe Fe XXIV and SDO/AIA 131 Å (Fe XXI) intensity maps, which have a peak sensitivity to 18 MK and 10 MK plasma, respectively. The red contours outline the regions where the EIS intensity is saturated and has unreliable temperature/density diagnostics. Also, note the “X”-shaped artificial diffraction pattern in EIS and AIA images. (e)–(h) Distribution of plasma density n_{th} , temperature T , magnetic field strength B , and vertical component of the plasma velocity v_y from the MHD model. (i)–(l) Distribution of nonthermal electrons at 50 keV, 100 keV, 200 keV, and 500 keV, respectively, from the particle model. Black curves in all panels are magnetic field lines derived from the MHD model.

at all energies are strongly concentrated in the magnetic bottle region. As discussed in the main text, we can draw an electron distribution function at each pixel of the model. Figure 8(c) shows examples from four selected locations. All the electron spectra display a power-law shape in the $\sim 30\text{--}600$ keV range, with those in the magnetic bottle region featuring a downward spectral break. Such broken power-law electron distributions in the model are formed by the combination of stochastic acceleration, trapping, and escaping processes (Kong et al. 2019; Li et al. 2022). The presence of a downward-breaking electron spectrum in the ALT magnetic bottle region is further supported by recent observations of the same flare during its early impulsive phase using combined EUV, X-ray, and microwave data (Chen et al. 2021).

D. EMISSION MODELING

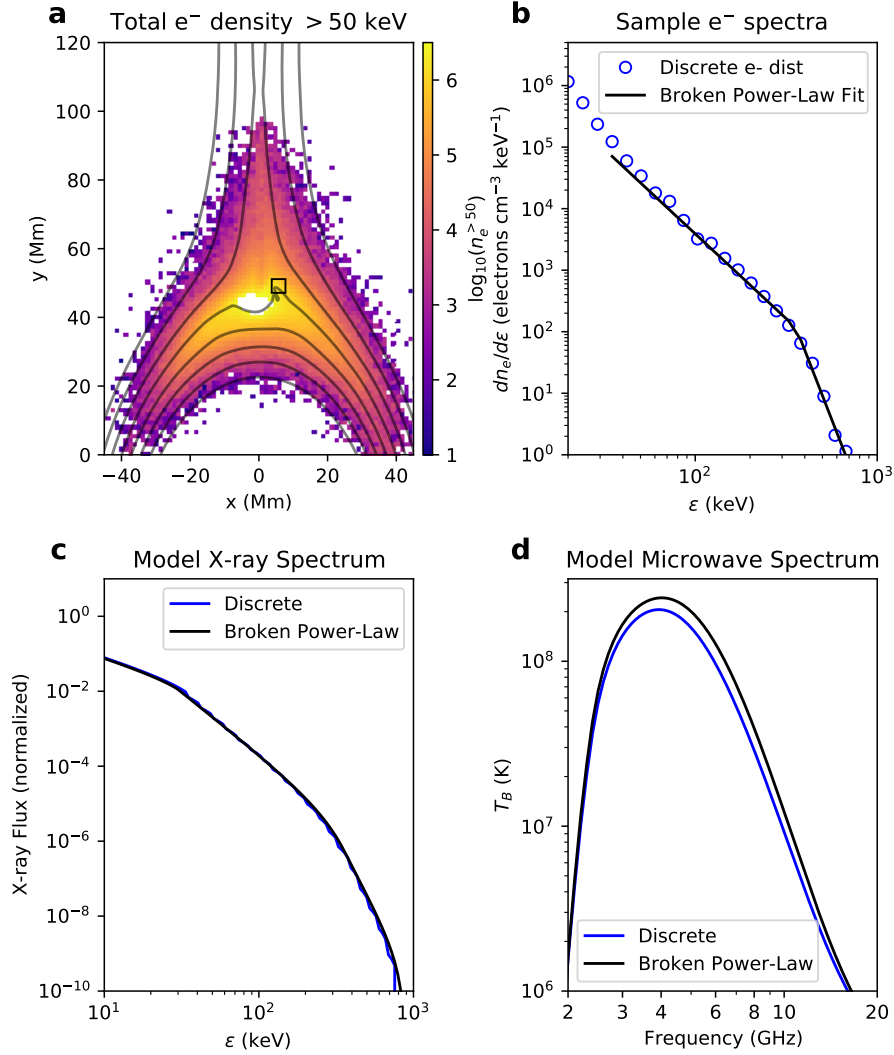


Figure 13. Modeled energetic electron distribution and calculated hard X-ray and microwave spectra. (a) Distribution of >50 keV energetic electrons from the combined MHD and particle model. (b) Electron distribution from a sample pixel in the model (black box in (a)). Blue circles are the distribution from the model, and the black curve shows the broken power-law fit. (c) Calculated X-ray spectra based on the bremsstrahlung mechanism. Blue and black curves are those using direct integration of the discrete electron distribution and the broken power-law fit, respectively. (d) Similar to (c), but for the calculated microwave spectra based on gyrosynchrotron radiation.

With maps of the thermal plasma properties and nonthermal electron distributions, one can calculate synthetic emission maps at various wavelengths and compare them with actual observations. To produce the synthetic SDO/AIA 131 Å EUV map, we only need the plasma density n_{th} and temperature T from the 2.5-D MHD model. We first calculate the EUV intensity at each pixel with $I(x, y) = n_{\text{th}}^2(x, y)G[T(x, y)]L_z$, where $G(T)$ is the temperature response function of the 131 Å band (O'Dwyer et al. 2010) and L_z is the line of sight depth (fixed to be 10 Mm where flare-heated, > 8 MK plasma is present and 1 Mm elsewhere to suppress the coronal background with an artificially high density as it is not optimized in the model), and then convolve the resulting image using a Gaussian kernel with a full width at half maximum (FWHM) width of $1''.2$ according to AIA's point spread function (PSF). Although we do not have sufficient information on the third dimension (along the line of sight) and hence have to use a homogeneous assumption, the resulting EUV 131 Å map, shown in Figure 8(e), resembles the observations reasonably well (Figure 8(f)).

In order to produce synthetic HXR and microwave maps, both the thermal plasma properties and nonthermal electron distributions are needed. For calculating synthetic HXR maps, at each pixel, we take the plasma density in the MHD model $n_{\text{th}}(x, y)$ and the nonthermal electron distribution $dn_e(x, y, \varepsilon)/d\varepsilon$ and compute the X-ray photon flux $I_X(x, y, \varepsilon)$ as a function of X-ray photon energy ε based on the thin-target bremsstrahlung theory. To perform the numerical calculations, we have adopted two commensurable approaches. One approach is to first fit the discrete nonthermal electron distribution from the particle model with a broken power-law form, and then supply the best-fit broken power-law function as the input to calculate the expected thin-target bremsstrahlung spectrum using existing tools available from the `xray` package within the `sswIDL` distribution². Another approach is, for every given X-ray photon energy ε , we take the discrete model electron distribution and integrate the X-ray flux contributed by all energy bins numerically. Figure 13(b) shows an example electron distribution derived from a selected pixel in the magnetic bottle region. Blue symbols are the discrete distribution from the particle model, and the black solid line is the best-fit broken power-law function. The calculated X-ray photon spectra using direct integration and broken power-law fit of the electron distribution are shown in panel (c) as blue and black curves, respectively. The results show that they are in agreement with each other.

For calculating the synthetic microwave spectrum from each pixel, we use the numerical codes developed by Kuznetsov & Fleishman (2021), which allows an input electron distribution in both the discrete numerical form and an analytical broken power-law form. Likewise, the results from the two different approaches are generally consistent with each other, although we found that the broken power-law approach gives better-defined microwave spectra as it effectively “smooths out” the occasional noise in the input electron distribution, especially in regions with low counting statistics. Therefore, we have adapted the broken power-law fit method to calculate the HXR and microwave spectra pixel-by-pixel, forming the spectrally resolved HXR and microwave maps. Finally, to compare with the observations, each image is convolved with a Gaussian function with the same FWHM width as the point spread function used to reconstruct the observed RHESSI and EOVSA images ($6''.8$ for RHESSI and $10''.2/[\nu/10 \text{ GHz}]$ for EOVSA).

REFERENCES

- Aschwanden, M. J., Hudson, H., Kosugi, T., & Schwartz, R. A. 1996a, *ApJ*, 464, 985
- Aschwanden, M. J., Kosugi, T., Hudson, H. S., Wills, M. J., & Schwartz, R. A. 1996b, *ApJ*, 470, 1198
- Aurass, H., & Mann, G. 2004, *ApJ*, 615, 526
- Aurass, H., Vršnak, B., & Mann, G. 2002, *A&A*, 384, 273
- Bárta, M., Büchner, J., Karlický, M., & Skála, J. 2011, *ApJ*, 737, 24
- Cai, Q., Shen, C., Raymond, J. C., et al. 2019, *MNRAS*, 489, 3183
- Caspi, A., Seaton, D., Casini, R., et al. 2023, in *Bulletin of the American Astronomical Society*, Vol. 55, 048
- Chen, B., Bastian, T. S., Shen, C., et al. 2015, *Science*, 350, 1238
- Chen, B., Battaglia, M., Krucker, S., Reeves, K. K., & Glesener, L. 2021, *ApJL*, 908, L55
- Chen, B., Shen, C., Reeves, K. K., Guo, F., & Yu, S. 2019, *ApJ*, 884, 63
- Chen, B., Yu, S., Reeves, K. K., & Gary, D. E. 2020a, *ApJL*, 895, L50
- Chen, B., Shen, C., Gary, D. E., et al. 2020b, *Nature Astronomy*, 4, 1140
- Chen, B., Gary, D., Yu, S., et al. 2023, in *Bulletin of the American Astronomical Society*, Vol. 55, 060
- Chen, Q., & Petrosian, V. 2013, *ApJ*, 777, 33

² Description of the software codes can be found at: https://hesperia.gsfc.nasa.gov/ssw/packages/xray/doc/brm_thin_doc.pdf

- Christe, S., Shih, A. Y., Dennis, B. R., et al. 2016, in AAS/Solar Physics Division Meeting, Vol. 47, AAS/Solar Physics Division Abstracts #47, 8.02
- Culhane, J. L., Harra, L. K., James, A. M., et al. 2007, *SoPh*, 243, 19
- Drake, J. F., Swisdak, M., Che, H., & Shay, M. A. 2006, *Nature*, 443, 553
- Dresing, N., Warmuth, A., Effenberger, F., et al. 2021, *A&A*, 654, A92
- Dulk, G. A., & Marsh, K. A. 1982, *ApJ*, 259, 350
- Fermi, E. 1949, *Physical Review*, 75, 1169
- Fleishman, G. D., & Kuznetsov, A. A. 2010, *ApJ*, 721, 1127
- Fleishman, G. D., Nita, G. M., Chen, B., Yu, S., & Gary, D. E. 2022, *Nature*, 606, 674
- Fletcher, L., & Martens, P. C. H. 1998, *ApJ*, 505, 418
- Fletcher, L., Dennis, B. R., Hudson, H. S., et al. 2011, *SSRv*, 159, 19
- Forbes, T. G. 1986, *ApJ*, 305, 553
- Foreman-Mackey, D., Hogg, D. W., Lang, D., & Goodman, J. 2013, *PASP*, 125, 306
- French, R. J., Yu, S., Chen, B., Shen, C., & Matthews, S. A. 2024, *MNRAS*, 528, 6836
- Gary, D., Chen, B., White, S., et al. 2023, in *Bulletin of the American Astronomical Society*, Vol. 55, 123
- Gary, D. E., Chen, B., Dennis, B. R., et al. 2018, *ApJ*, 863, 83
- Giacalone, J., & Jokipii, J. R. 1999, *ApJ*, 520, 204
- Ginzburg, V. L., & Syrovatskii, S. I. 1965, *ARA&A*, 3, 297
- Goodman, J., & Weare, J. 2010, *Communications in Applied Mathematics and Computational Science*, 5, 65
- Guidoni, S. E., Karpen, J. T., & DeVore, C. R. 2022, *ApJ*, 925, 191
- Guo, F., & Giacalone, J. 2012, *ApJ*, 753, 28
- Hayes, L. A., Gallagher, P. T., Dennis, B. R., et al. 2019, *ApJ*, 875, 33
- Hurford, G. J., Schmahl, E. J., Schwartz, R. A., et al. 2002, *SoPh*, 210, 61
- Ishikawa, S., Krucker, S., Takahashi, T., & Lin, R. P. 2011, *ApJ*, 737, 48
- Karlický, M., & Kosugi, T. 2004, *A&A*, 419, 1159
- Kliem, B., Karlický, M., & Benz, A. O. 2000, *A&A*, 360, 715
- Kong, X., Guo, F., Shen, C., et al. 2020, *ApJL*, 905, L16
- . 2019, *ApJL*, 887, L37
- Kong, X., Ye, J., Chen, B., et al. 2022a, *ApJ*, 933, 93
- Kong, X., Chen, B., Guo, F., et al. 2022b, *ApJL*, 941, L22
- Kontar, E. P., Bian, N. H., Emslie, A. G., & Vilmer, N. 2014, *ApJ*, 780, 176
- Kontar, E. P., Perez, J. E., Harra, L. K., et al. 2017, *PhRvL*, 118, 155101
- Krucker, S., & Battaglia, M. 2014, *ApJ*, 780, 107
- Krucker, S., Hudson, H. S., Glesener, L., et al. 2010, *ApJ*, 714, 1108
- Krucker, S., Kontar, E. P., Christe, S., & Lin, R. P. 2007, *ApJL*, 663, L109
- Kuznetsov, A. A., & Fleishman, G. D. 2021, *ApJ*, 922, 103
- Lemen, J. R., Title, A. M., Akin, D. J., et al. 2012, *SoPh*, 275, 17
- Li, X., Guo, F., Chen, B., Shen, C., & Glesener, L. 2022, *ApJ*, 932, 92
- Li, X., Guo, F., Li, H., & Li, S. 2018, *ApJ*, 866, 4
- Lin, J., & Forbes, T. G. 2000, *J. Geophys. Res.*, 105, 2375
- Lin, R. P. 1974, *SSRv*, 16, 189
- Lin, R. P., Dennis, B. R., Hurford, G. J., et al. 2002, *SoPh*, 210, 3
- Litvinenko, Y. E. 1996, *ApJ*, 462, 997
- Liu, R. 2013, *MNRAS*, 434, 1309
- Longcope, D., & Qiu, J. 2022, *ApJ*, 941, 160
- Longcope, D., Qiu, J., & Brewer, J. 2016, *ApJ*, 833, 211
- Longcope, D., Unverferth, J., Klein, C., McCarthy, M., & Priest, E. 2018, *ApJ*, 868, 148
- Longcope, D. W., & Guidoni, S. E. 2011, *ApJ*, 740, 73
- Luo, Y., Chen, B., Yu, S., Bastian, T. S., & Krucker, S. 2021, *ApJ*, 911, 4
- Mann, G., Veronig, A. M., & Schuller, F. 2024, *arXiv e-prints*, arXiv:2404.12005
- Mann, G., Warmuth, A., & Aurass, H. 2009, *A&A*, 494, 669
- Martens, P. C. H. 1988, *ApJL*, 330, L131
- Masuda, S., Kosugi, T., Hara, H., Tsuneta, S., & Ogawara, Y. 1994, *Nature*, 371, 495
- O'Dwyer, B., Del Zanna, G., Mason, H. E., Weber, M. A., & Tripathi, D. 2010, *A&A*, 521, A21
- Parker, E. N. 1965, *Planet. Space Sci.*, 13, 9
- Polito, V., Galan, G., Reeves, K. K., & Musset, S. 2018, *ApJ*, 865, 161
- Reeves, K. K., Polito, V., Chen, B., et al. 2020, *ApJ*, 905, 165
- Reeves, K. K., Warren, H. P., & Forbes, T. G. 2007, *ApJ*, 668, 1210
- Ruan, W., Yan, L., & Keppens, R. 2023, *ApJ*, 947, 67
- Schwartz, R. A., Csillaghy, A., Tolbert, A. K., et al. 2002, *SoPh*, 210, 165
- Shen, C., Chen, B., Reeves, K. K., et al. 2022, *Nature Astronomy*, 6, 317
- Shen, C., Kong, X., Guo, F., Raymond, J. C., & Chen, B. 2018, *ApJ*, 869, 116
- Shen, C., Polito, V., Reeves, K. K., et al. 2023, *Frontiers in Astronomy and Space Sciences*, 10, 19
- Shibata, K., Takasao, S., & Reeves, K. K. 2023, *ApJ*, 943, 106

- Somov, B. V., & Kosugi, T. 1997, *ApJ*, 485, 859
- Takasao, S., Matsumoto, T., Nakamura, N., & Shibata, K. 2015, *ApJ*, 805, 135
- Takasao, S., & Shibata, K. 2016, *ApJ*, 823, 150
- Tandberg-Hanssen, E., & Emslie, A. G. 1988, *The physics of solar flares*
- Tsuneta, S., & Naito, T. 1998, *ApJ*, 495, L67
- Veronig, A. M., & Brown, J. C. 2004, *ApJL*, 603, L117
- Wang, M., Chen, B., Yu, S., et al. 2023a, *ApJ*, 954, 32
- Wang, W., Wang, L., Krucker, S., et al. 2021, *ApJ*, 913, 89
- Wang, Y., Cheng, X., Ding, M., et al. 2023b, *ApJL*, 954, L36
- Warren, H. P., Brooks, D. H., Ugarte-Urra, I., et al. 2018, *ApJ*, 854, 122
- Yan, X. L., Yang, L. H., Xue, Z. K., et al. 2018, *ApJL*, 853, L18
- Ye, J., Cai, Q., Shen, C., et al. 2020, *ApJ*, 897, 64
- Yu, S., Chen, B., Reeves, K. K., et al. 2020, *ApJ*, 900, 17